PHOTONICS Research

Multimode vibrational strong coupling in direct laser written mid-IR plasmonic MIM nano-patch antennas

Nicholas V. Proscia,[1,*] Michael A. Meeker,[1] Nicholas Sharac,[1,3] Frank K. Perkins,[2] Chase T. Ellis,[2] Paul D. Cunningham,[2] and Joseph G. Tischler[2,4]

[1]NRC Postdoc residing at U.S. Naval Research Laboratory, Washington, D.C. 20375, USA
[2]U.S. Naval Research Laboratory, Washington, D.C. 20375, USA
[3]Current address: Rigetti Computing, Freemont, California 94538, USA
[4]Current address: Homer L. Dodge Department of Physics and Astronomy, The University of Oklahoma, Norman, Oklahoma 73019, USA
*Corresponding author: nicholas.proscia@nrl.navy.mil

Received 14 July 2023; revised 24 September 2023; accepted 7 October 2023; posted 11 October 2023 (Doc. ID 500339); published 24 November 2023

Strong coupling of mid-infrared (mid-IR) vibrational transitions to optical cavities provides a means to modify and control a material's chemical reactivity and offers a foundation for novel chemical detection technology. Currently, the relatively large volumes of the mid-IR photonic cavities and weak oscillator strengths of vibrational transitions restrict vibrational strong coupling (VSC) studies and devices to large ensembles of molecules, thus representing a potential limitation of this nascent field. Here, we experimentally and theoretically investigate the mid-IR optical properties of 3D-printed multimode metal–insulator–metal (MIM) plasmonic nanoscale cavities for enabling strong light–matter interactions at a deep subwavelength regime. We observe strong vibration-plasmon coupling between the two dipolar modes of the L-shaped cavity and the carbonyl stretch vibrational transition of the polymer dielectric. The cavity mode volume is half the size of a typical square-shaped MIM geometry, thus enabling a reduction in the number of vibrational oscillators to achieve strong coupling. The resulting three polariton modes are well described by a fully coupled multimode oscillator model where all coupling potentials are non-zero. The 3D printing technique of the cavities is a highly accessible and versatile means of printing arbitrarily shaped submicron-sized mid-IR plasmonic cavities capable of producing strong light–matter interactions for a variety of photonic or photochemical applications. Specifically, similar MIM structures fabricated with nanoscopic voids within the insulator region could constitute a promising microfluidic plasmonic cavity device platform for applications in chemical sensing or photochemistry. © 2023 Chinese Laser Press

https://doi.org/10.1364/PRJ.500339

1. INTRODUCTION

Surface plasmon modes hosted by noble metals, their nanostructures, and metamaterials are now routinely used to influence light–matter interactions. The resulting confinement and enhancement of local electromagnetic fields lead to surface enhancement of Raman scattering [1], infrared (IR) absorption [2], and nonlinear optical phenomena [3], while an increase in the vacuum density of states leads to Purcell enhancement of fluorescence [4]. Metal–insulator–metal (MIM) plasmonic structures, including MIM waveguides, nanoparticle-on-mirror, nanogap cavities, and patch antennas, have emerged as a versatile platform for extreme subwavelength confinement of electromagnetic radiation, offering reduced losses and orders of magnitude stronger fields over a large bandwidth ranging from the visible to the mid-IR [5–8]. MIM structures work through mutual excitation of coherent localized surface plasmon modes on two metal interfaces separated by a thin dielectric layer leading to deep subwavelength plasmonic modes based on Maxwell's equations. These modes have a lower damping rate than single-interfaced surface plasmon polaritons (SPPs) [9,10], and when one or two of the interfaces are finite in size, an ultra-small volume cavity can be created without a cutoff wavelength [11]. As a result of the several orders of magnitude increase in field strength, MIM structures offer a host of interesting applications related to enhancing light–matter interactions, which include use in chemical sensing [12–14], quantum light sources [15,16], lasers [17], high-speed LEDs [18], and exploiting chiral interactions with matter [19,20].

When the light–matter interactions are large enough such that the exchange of energy between the photonic and material

system occurs at a faster rate than the energy dissipation, this interaction between the systems is said to be in the strong coupling regime [21,22]. In this regime, the light- and matter-state properties hybridize to produce new quasiparticles called polaritons [23] with novel behavior not present in either constituent system. The use of strong coupling to engineer new physical systems has proved invaluable in many areas of fundamental research [24,25]. While much of the past work has focused on modifying electronic transitions [23,26–29], many recent efforts have been focused on vibrational strong coupling (VSC), in which molecular vibrational transitions are strongly coupled to photonic or plasmonic structures [30–35]. The goals of such research include realizing ultrasensitive bio and chemical sensors, modifying chemical properties of materials, producing supramolecular assembly of polymers [36], and controlling thermal emissivity of material systems [33,37–39]. Due to the low oscillator strength of vibrational modes, it is difficult to achieve VSC via localized surface plasmon resonances that confine fields in three dimensions. Therefore, open plasmonic systems with confinement only along one or two dimensions are often employed to reach the VSC regime as they can incorporate a larger number of oscillators, enhancing the coupling strength since this quantity scales according to the square root of the number of oscillators [40,41]. Recently, a plasmonic MIM nanogap closed-cavity design was employed to realize VSC by increasing the light–matter coupling strength via its ultra-high field confinement [42]. Such MIM structures are typically fabricated via 2D electron beam lithography techniques that can be time consuming and costly while placing limits on the complexity of the three-dimensional structures that can be realized.

In this study, we use direct laser writing of 3D nanostructures to create L-shaped MIM nanogap cavities with fundamental resonances in the mid-IR. This fast and inexpensive fabrication technique enables rapid prototyping and evaluation of photonic systems of arbitrary shape and complexity within its printable size range [43,44]. In prior work, anisotropic L- and V-shaped plasmonic nanoparticles and their inverse, apertured plasmonic films, have proven to be a versatile platform for the manipulation of the near and far fields of incident light, which includes enhancement of birefringence [45], wideband polarization conversion [46,47], optical phased arrays [48], as well as circular dichroism [49]. Here, we apply this class of structure, specifically the L-shaped geometry with two orthogonal oscillator arms, in a nanogap MIM geometry to confine the composite resonances primarily within the insulator volume. These L-shaped cavities are studied as a function of arm length and polarization angle. We find that the expressed modes of the plasmonic system are the dipolar bonding and antibonding modes that result from hybridization of the fundamental resonances of each individual arm [49]. The subwavelength field enhancement produces strong coupling between the dipolar modes from each arm of the cavity to the carbonyl (-C=O) stretch vibrational transition (CSVT) in the acrylate-based polymer insulator [30].

Further, we find that the strongly coupled light–matter system can only be fully understood through a multimode three-oscillator model where coupling is non-zero for all three pair-wise interactions of the constituent modes, e.g., between the two fundamental dipolar modes of each individual arm as well as between each of those modes and the CSVT of the polymer insulator. This is because the coupling strength between the modes of the two individual arms affects the observed Rabi splitting with the CSVT of the polymer. The resulting avoided crossings are less intuitive and cannot be reproduced if the Hamiltonian is simplified to include only two coupling terms, either as is typically done for multimode systems that have been previously studied [50–52] or by treating the system as a simpler two-oscillator model, e.g., coupling between the resulting cavity bonding mode and the CSVT. Such systems are essentially described by one or two pair-wise interactions, whereas the system we have examined is better described by three pair-wise coupled oscillators. The large coupling potential between the two cavities' modes produces an extremely large Rabi splitting of 1101 cm^{-1} between the upper and lower polariton branches. The Rabi splitting between the lower and middle polariton branches reaches 104 cm^{-1}, placing it within the strong coupling regime for light–matter coupling to mid-IR vibrational transitions of materials. This strong coupling is achieved with less than half the cavity volume of a typical square MIM cavity [42], indicating a large increase in field confinement that compensates for the reduction in the number of vibrational oscillators. As such, these direct laser written MIM structures are a promising platform to explore the effects of VSC in chemical and plasmonic systems. In particular, inclusion of nanoscopic channels in the insulator region would allow for fluid flow to enable microfluidic plasmonic cavity devices for photochemistry applications.

2. RESULTS

The L-shaped nanogap cavities were fabricated via directing lasing writing, using a Nanoscribe Photonic Professional GT laser lithography system, where two-photon polymerization enables 3D printing of nanometer-sized structures [43]. A flow chart of the fabrication steps can be seen in Fig. 1(a). First, a 150 nm Au film was coated onto a silicon substrate by electron beam evaporation at pressures below 10^{-8} Torr (1 Torr = 133.32 Pa), to ensure a high-optical-quality Au film thicker than the penetration depth, therefore fully reflective in the wavelength range of interest. Subsequently the Nanoscribe-proprietary photoresist, IP-Dip, was drop casted on top of the Au film, and 200 μm by 200 μm arrays of the same size L-shaped nanostructure with a constant 1600 nm pitch were written using the piezo mode, which corrects for tilting of the substrate. Multiple arrays were printed in which the arm length of the L was varied to investigate its effect on the resonance energy and polarization. After writing and development of the exposed IP-Dip resist, a film of 70 nm Au was deposited by electron beam evaporation on top, creating an L-shaped MIM nanogap cavity. The shape and dimensions of the L-cavities are shown in Fig. 1(b). The X- and Y-arm lengths, L_x and L_y, respectively, along each axis were independently varied from a nominal length of 600 nm to 1400 nm in increments of ∼200 nm. The widths of the L structures were kept to a nominal 300 ± 15 nm. The cavity thickness was kept constant at 150 nm. Their shapes and dimensions were confirmed using scanning electron

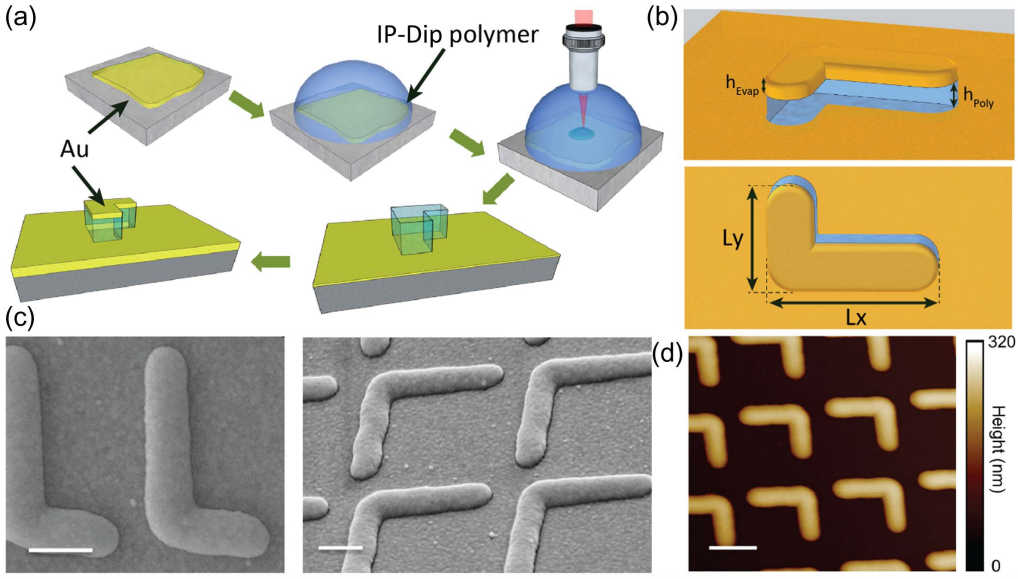

Fig. 1. Fabrication details and material characterization of the MIM L-cavities. (a) Flow diagram of the fabrication process involved in direct laser writing of the MIM L-cavities. (b) Graphic of the final L-cavities used in EM simulations; top, angled side profile; bottom, angled overhead view. (c) SEM image of a fabricated L-cavity with arm lengths of 795 nm and 1324 nm (left). 45° image of similar L-cavities (right). Scale bars represent 400 nm. (d) AFM height image of a similar set of L-cavities. Scale bar represents 1000 nm.

microscopy (SEM) and atomic force microscopy (AFM), as shown in Figs. 1(c) and 1(d).

The final MIM structures are shown in the SEM and AFM images of Figs. 1(c) and 1(d), respectively. From the SEM images, we find that the periodicity of the structures ranged from 1570 to 1610 nm where the nominal distance was 1600 nm. The nominal length of each arm was varied from 600 nm to 1400 nm in increments of 200 nm. The measured lengths were within 100 nm of the target length. Generally, the width of the cavity arms ranged from 290 to 320 nm and decreased as the arm length increased. From the AFM images, the height of the developed polymer was 150 nm with a radius of curvature (ROC) of 50 nm along the top edges of the L-cavity. The ROCs of the tips of L-cavities were approximately one half the width, while the ROC of the outer intersection of the arms was found to be 150 nm.

The optical response of a representative set of L-cavities is analyzed in Fig. 2, where Fig. 2(c) shows a series of polarization-resolved experimental reflectance spectra from an array of L-cavities with arm lengths $L_x = 797$ and $L_y = 1324$ nm. Each reflectance dip in the spectra corresponds to the absorption of a distinct plasmonic resonance. The origin of each mode can be understood from the numerical EM simulations of the structure. Figures 2(a) and 2(b) show the out-of-plane electric field (E_z) profiles of the simulated modes at 50 nm above the initial Au substrate. The L-cavity modes consist of a series of dipolar and higher-order resonances, labeled modes L, M, U, and H1–H4 in Figs. 2(a) and 2(b). The resonant modes are created by in-phase LSPRs associated with the two interfaces created by the Au substrate and the 70 nm thick evaporated Au film on top of the IP–Dip polymer. The change in impedance at the edges of the structures confines the mode in the lateral dimensions [7]. For each of these modes, the electric field is primarily normal to the substrate (E_z) with significant in-plane (E_x and E_y) components only occurring from the fringe fields at the edges of the structure (see Fig. 5 in Appendix A).

The lowest-energy out-of-plane dipolar modes, labeled L, M, and U, are polariton modes that originate from VSC between the dipolar plasmonic resonances of each individual arm and the CSVT of the IP-Dip polymer, located at 1732 cm^{-1}. They will be the focus of this work and will be described in depth in what follows. The out-of-plane electric field (E_z) profiles in Fig. 2(a) show that mode U has an antibonding-like character while modes L and M have bonding-like characters, with dipole moments oriented at 22° and 110° relative to the x-axis, respectively, shown in Fig. 2(d). At larger wavenumbers, the resonances of the structure come from higher-order plasmon modes shown in Fig. 2(b) for modes H1–H4. Mode H1 is another antibonding-like mode with an additional node at the tip of the L_y arm leading to a slight rotation in the dipole direction to 30° [Fig. 2(e)]. Mode H2 corresponds to a second-order resonance nearly along the x-axis, producing resonant field oscillations along the width of the Y-arm as well as the length of the X-arm, L_x. Mode H3 is an asymmetric mode nearly orthogonal to mode H2, producing field oscillations along the width of the X-arm as well as the Y-arm length, L_y. Mode H4 is a superposition of higher-order resonances along both the x- and y-directions. All localized modes of the L-cavities were independent of the incident angle of illumination, implying that scattering is the primary mechanism for coupling to the incident light [42]. There are several other higher-order modes (at 4400 cm^{-1}, 5750 cm^{-1}, and 6050 cm^{-1}) that are not visible in the experimental reflectance data in Fig. 2(c) (upper) but are predicted by the EM simulation in Fig. 2(c) (lower). Of note is the mode at 4400 cm^{-1} that is nearly degenerate with H1, and may overlap with H1 in the

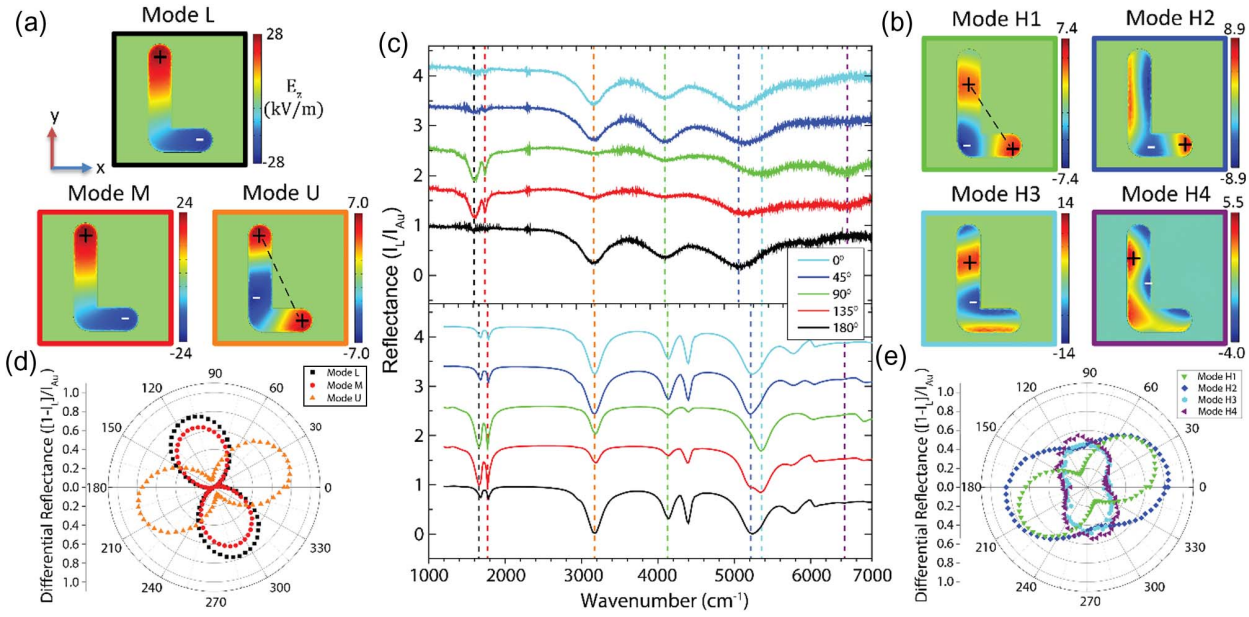

Fig. 2. Modal analysis of the L-cavity resonances. (a), (b) Simulated out-of-plane electric field (E_z) profiles of the modes identified in the polarization-resolved reflectance spectra in (c). The modes are color-coded according to the border color of each plot. (c) Experimental (upper) and simulated (lower) polarization-resolved reflectance spectra. The polarization angle of each measurement is indicated in the legend, and the spectral locations of the modes are outlined by the color-coded dashed lines. The spectra in waterfall plots are separated by increments of 0.8. (d), (e) Polar plots of the differential experimental reflectance of the modes shown in (a)–(c). I_{Au} and I_L are the reflected intensities from a planar Au film and L-cavity array with arm lengths of $L_x = 797$ nm and $L_y = 1324$ nm, respectively.

experimental data due to linewidth-width broadening in the fabricated cavities. The field profiles of these higher-order modes are plotted in Fig. 6 for completeness (see Appendix A). Please note that these higher-order modes (H1–H4) are not the focus of the rest of this report as they do not play a significant role in the light–matter coupling experienced by the CSVT and the cavity.

The lowest-energy modes of the L-shaped cavity can be understood within the conductively coupled oscillator interpretation, where each arm of the cavity can be treated as an independent oscillator that couple together [see Fig. 8(c) in Appendix B] to produce orthogonal bonding and antibonding modes [49] orthogonal to one another. VSC between the dipolar plasmonic resonances of each individual arm and the CSVT of the IP-Dip polymer leads to what would have been the cavity bonding and antibonding modes (see Fig. 9 in Appendix B) to split into lower (L), middle (M), and upper (U) polaritons branches. In this context, modes L and M take the character of the dipolar bonding mode, where the charge within each arm oscillates in-phase leading to destructive interference at the intersection of the two arms. Mode U has primarily an antibonding character, where the charges in both arms oscillate out-of-phase with each other creating constructive interference at the intersection of two arms. This interpretation is consistent with the differential reflection polar plots of Fig. 2(d), where modes L and M have a dipole moment of 110° relative to the x-axis and mode U is nearly orthogonal with a dipole moment oriented 22° relative to the x-axis.

The multimode VSC in the system takes place between the two dipolar modes associated with each arm of the cavity [see Fig. 8(c) in Appendix B] and the CSVT of the IP-Dip polymer, resulting in three hybrid light–matter polariton modes. Figure 3(a) shows a waterfall plot of the experimental reflectance spectra of the three polariton modes for various L_x. L_y was kept nearly constant with a mean of 760 nm while L_x was varied between 600 nm and 1400 nm in steps of ∼200 nm. The measured arm lengths obtained from SEM images are displayed in the legend of Fig. 3(a). In the experimental reflectance of Fig. 3(a), an avoided-crossing between modes L and M is clearly visible as well as a second avoided-crossing between modes U and M, thus indicating that modes L, M, and U are three branches of a single multimode polariton system.

To model such a multimode system, one employs a coupled 3 × 3 linear matrix, Eq. (B3), with its eigenvalues characterizing the three polariton branches (modes L, M, U). The coupling strengths are given by the interaction potentials $V_{1,2}$, where V_1 is the potential between the two cavity modes, $\omega_x[x]$ and ω_y, while coupling strengths between the CSVT, ω_{vib}, and the cavity modes are given by V_2. A full derivation is given in Appendix B. By solving Eq. (B4) numerically and fitting the three eigenvalues, $\lambda_{L,M,U}$, to the measured resonances of each polariton branch shown in Figs. 3(a) and 3(c), we find the interaction potentials $V_{1,2}$ to equal 541 cm^{-1} and 82 cm^{-1}, respectively. Figure 7 in Appendix A shows agreement between numerical EM simulations of the system and experimental reflectance, indicating that both methods produce similar interaction potentials. From the resulting three coupled oscillator model, we determine the Rabi splitting between polariton branches L-M and M-U, to be 101 cm^{-1} and 1086 cm^{-1},

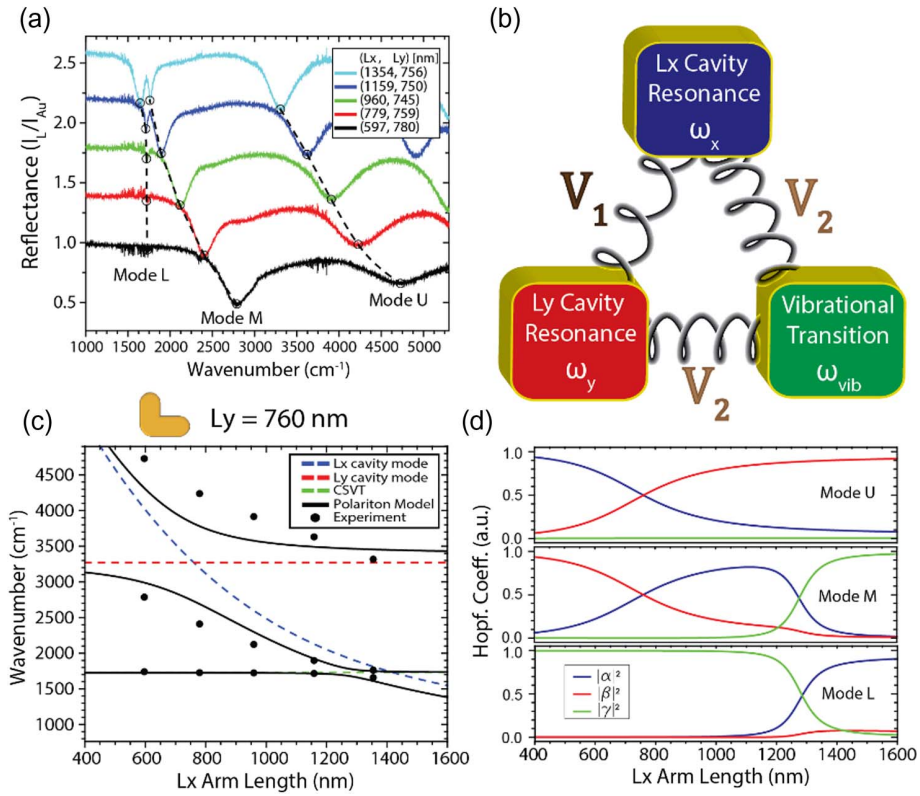

Fig. 3. Vibrational-plasmon strong coupling. (a) Experimental reflectance of modes L, M, and U in the frequency range where VSC to the IP-Dip vibrational mode occurs as the aspect ratio of the L is varied as a function of L_x. The dotted lines are guides to the eye indicating the polariton disperson. (b) Three-coupled-oscillator model where both cavity modes are coupled to each other as well as to a molecular vibration within the polymer. (c) Comparison between the measured location of the upper, middle, and lower polaritons in (a) (black circles) and the coupled three-oscillator model (black lines). The uncoupled L_x (blue) and L_y (red) modes predicted by Eq. (B1) and the vibrational transition (green) are given by the dashed lines. (d) Hopfield coefficents or the eigenvectors for the eigenvalues of the three-coupled-oscillator model in Eq. (B3) as a function of L_x.

which occur for L_x arm lengths of 1284 nm and 760.46 nm, respectively. A total splitting between L-U branches was found to be 1758.52 cm^{-1} occurring at 1210 nm. Directly measuring the Rabi oscillations associated with these splitting values via coherent ultrafast spectroscopy is beyond the scope of the current study. These two avoided-crossings appear to be nearly independent of each other. The M-U avoided-crossing appears to be dominated by coupling between the dipolar cavity modes of each arm of the L-shaped cavity. The L-M avoided-crossing appears to be dominated by strong light–matter interaction between the L_x arm dipolar mode of the cavity and the CSVT of the IP-Dip polymer. In this case, the mode dispersion predicted by the three coupled oscillator model is consistent with an intuitive understanding of two pair-wise coupled oscillators, where each crossing is essentially described by an independent two-coupled-oscillator interaction; see Fig. 10 in Appendix B.

The Hopfield coefficients or eigenvectors $\alpha[x], \beta[x], \gamma[x]$ of Eq. (B3), shown in Fig. 3(c), represent the weighted contribution of the original uncoupled modes $\omega_x[x], \omega_y, \omega_{\text{vib}}$ to each polariton branch, respectively. ω_y and ω_x are the energies of the plasmonic modes associated with each arm length L_x and L_y, respectively, and ω_{vib} is the energy of the CSVT. As the L_x increases in length, the U polariton goes from an almost pure ω_x mode to ω_y with a small contribution from ω_{vib}. The M polariton evolves from primarily ω_y character to a combination of the cavity modes and eventually approaches a pure ω_{vib} nature at larger arm lengths, while the L polariton goes from having a pure ω_{vib} mode character to mostly ω_x where the ω_y mode remains a small contribution.

To further understand the interplay between constituent modes ($\omega_x, \omega_y, \omega_{\text{vib}}$) and the behavior of the polariton branches, we apply the coupled oscillator model in Eq. (B3) to several different L_y lengths using the same $V_{1,2}$ values that were used to describe $L_y = 760$ nm. Figure 4 shows the experimental and modeled mode dispersion as a function of L_x for several different L_y values, while Fig. 11 (see Appendix C) shows the experimental reflectance data. As L_y is elongated, the dipolar mode ω_y red shifts towards the CSVT ω_{vib}. Mode M becomes pinned, as expected, between ω_y and ω_{vib}. As the energy differences among the three modes decrease, the interactions among the three modes become less independent and correspondingly less intuitive. Focusing on the behavior of the L and M polaritons, as L_y increases, the anti-crossing point shifts toward shorter L_x, away from the length where $\omega_y = \omega_{\text{vib}}$. This behavior clearly deviates from the typical pair-wise dominated coupled-oscillator interactions that give rise to avoided-crossings when any two uncoupled frequencies are resonant. Such pair-wise interactions among three oscillators are treated by only considering two of

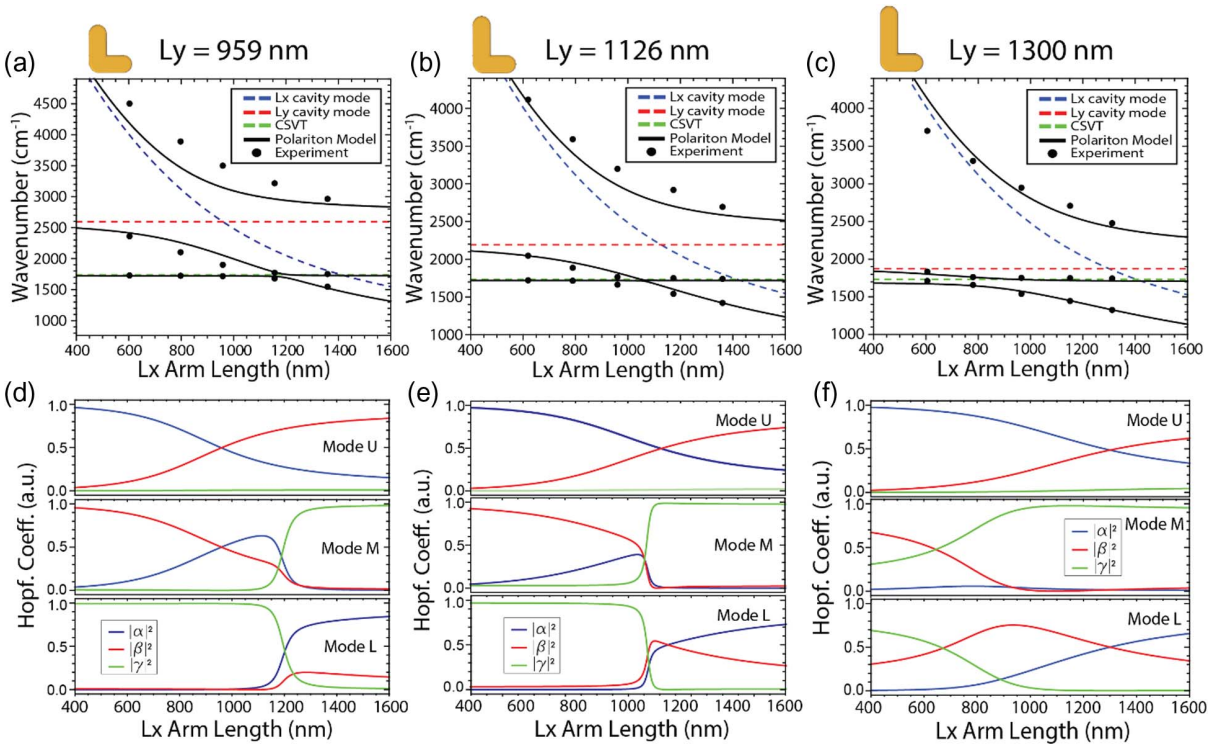

Fig. 4. Multimode coupling for various L_y arm lengths. (a)–(c) Experimentally measured location of the upper, middle, and lower polaritons (black circles) and the three-coupled oscillator model (black lines) for three different average L_y: (a) 959 nm, (b) 1126 nm, and (c) 1300 nm. The uncoupled L_x (blue) and L_y (red) modes predicted by Eq. (B1) and the vibrational transition (green) are given by the dashed lines. (d)–(f) Hopfield coefficents of the 3 × 3 oscillator model in Eq. (B3) as a function of L_x for an average L_y of (d) 959 nm, (e) 1126 nm, and (f) 1300 nm.

the three possible coupling terms. Here, the non-zero coupling among all three modes means that the observed behavior of the L and M polaritons depends on all three modes. The Rabi splitting between the L-M polaritons decreases as L_y is increased, reaching 53 cm^{-1} for $L_y = 959$ nm and 15 cm^{-1} for $L_y = 1126$ nm in Figs. 4(a) and 4(b) when the L-M anti-crossing point occurs for more symmetric L-cavities. Under these conditions, where $L_y = L_x$, ω_x and ω_y become resonant, and the exceptionally large plasmon–plasmon coupling causes both modes to strongly shift away from each other. Since $V_1 > V_2$, the U-M polariton avoided-crossing applies pressure to the L-M avoided-crossing, reducing its observed Rabi splitting so that the system is no longer in the strong coupling regime for these two cases and can be referred to as a strong interaction instead of strong coupling [53]. In Fig. 4(c), L_y is further increased to 1300 nm, and the Rabi splitting again increases to 104 cm^{-1}. Therefore, asymmetric L shapes produce a larger Rabi splitting than symmetric L shapes for the L-M polaritons in this particular regime where $\omega_y > \omega_{vib}$; this does not hold when $\omega_y < \omega_{vib}$. From how the resulting polariton modes, particularly the L and M branches, depend on the three constituent plasmonic and vibrational modes, we see that only through a multimode coupling model where all three coupling strengths are accounted for can the system be fully understood and its behavior predicted.

From Figs. 3(c), 4(d), and 4(e), we can see how the character of each polariton branch changes as L_x and L_y are varied. When L_y is elongated (i.e., ω_y decreases in energy), the U polariton crossover point from $\omega_x \rightarrow \omega_y$ character shifts to longer values of L_x as expected since the condition $\omega_y = \omega_x$ determines this crossover point. Furthermore, the contribution of ω_{vib} (although small) increases for longer L_y lengths because ω_y generally sets the lower limit for the energy of the U polariton in this regime and so as ω_y decreases, the U polariton is allowed to approach closer to ω_{vib} and inherit more of its character. For shorter L_y arm lengths, the M polariton evolves along $\omega_y \rightarrow \omega_x \rightarrow \omega_{vib}$ in character as L_x increases. As L_y lengthens and ω_y decreases in energy, the ω_y contribution to the M polariton begins to dominate the ω_x contribution and the M polariton transitions from ω_y to ω_{vib} with L_x. Changes in L_y have nearly the opposite effect on the character of the L polariton. Here, its character evolves from mostly ω_{vib} to ω_x with L_x for shorter L_y to a transition through $\omega_{vib} \rightarrow \omega_y \rightarrow \omega_x$ with L_x for longer L_y because the ω_y contribution to the L polariton becomes more significant as ω_y decreases in energy. From the analysis above, we see that controlling the different aspect ratios of the L-cavities offers a way to tune the behavior and character of these modes.

It is tempting to try to describe the system by two cascaded two-oscillator models: the first to describe the plasmon–plasmon interaction of the cavity arms to create the bonding and antibonding modes, and second to describe the plasmon–vibration interaction of the cavity bonding mode with the CSVT. Shown in Fig. 10(a), we apply a two-coupled-oscillator model between only the cavity bonding mode and CSVT $L_y = 959$ nm, where there remains a large energy detuning of the U mode with respect to ω_{vib}. This model leads to

a lower value of V_2 than that we obtained using the three-oscillator model (23 cm^{-1} for $L_y = 959$). For longer L_y, Fig. 10 (b), we start to recover the V_2 value (63 cm^{-1}) as found in the three-oscillator model when the bonding mode is becoming dominated by the resonance in a single arm. So we see that a two-oscillator model between the resulting bonding mode and CSVT is insufficient as it requires large changes to the interaction potential, V_2. The multimode VSC model recovers this change in the observed splitting while keeping the interaction potentials, V_1 and V_2, constant for all aspect ratios, as expected for the different aspect ratios of the cavities.

3. DISCUSSION

Plasmon-vibration coupling between the MIM L-cavity modes and the CSVT of the IP-Dip polymer fundamentally modified these two separate systems into a single new hybrid light–matter system with the three polariton eigenmodes given by Eq. (B3). Evaluating the coupling strength of multiple coupled oscillators is less straightforward than the case of a simple two-oscillator system. The Rabi splitting of 1758.52 cm^{-1} between the U and L polariton bands for $L_y = 759$ nm clearly meets the proposed criteria [54] for strong multimode coupling as it is larger than the weighted average of the linewidths of the polariton branches of 250 cm^{-1}. In fact, this meets the criteria for ultrastrong coupling because the Rabi splitting is on the order of the bare cavity frequency, the reduced coupling strength is >10%, and the geometric mean between the reduced coupling strength and cooperativity factor exceeds unity. However, since the U and L polaritons are dominated by a plasmonic character for the relevant arm lengths, the U-L Rabi splitting may not be representative of the light–matter coupling, but may be better understood as dominated by plasmon–plasmon coupling.

If we instead judge the plasmon-vibration coupling based on the L-M Rabi splitting, as these modes retain the most vibrational mode character, then we see that the Rabi splitting is larger than the polariton linewidths, so that the system may be described by the strong coupling regime. A number of criteria for strong light–matter coupling are used in the literature based on the strength of the coupling interaction potential, the Rabi splitting, and the linewidth. The less strict criteria based on the simple two-coupled-oscillator model in the absence of damping require that twice the interaction potential, i.e., $2V_2$, be larger than the average linewidths. However, merely meeting this criterion produces no visible Rabi splitting. Since broadening reduces the observed Rabi splitting, the condition for visibility is that the Rabi splitting should be larger than the average linewidths [26]. The uncoupled CSVT linewidth was measured to be 32 cm^{-1} from reflectance spectra of bare IP-Dip on an Au substrate, as shown in Fig. 12 in Appendix C. The uncoupled plasmonic linewidth was determined experimentally by measuring the FWHM of mode M when it is of a primarily plasmonic character and via numerical simulations when the CSVT was removed from the IP-Dip dielectric function. The linewidths in each case are 163 cm^{-1} and 142 cm^{-1}, respectively. Thus, the averaged linewidth of the uncoupled oscillators (98 cm^{-1} via experimental data) is smaller than the Rabi splitting (104 cm^{-1} and 101 cm^{-1}) for cavities where $L_y = 1300$ nm and $L_y = 760$ nm, respectively [27]. Therefore, these asymmetric systems meet the criteria for strong light–matter coupling. So through this demonstration, we see that this 3D printed MIM L-shaped cavity can achieve strong plasmon-vibration coupling if properly tuned with respect to a vibrational transition of interest.

The observed VSC and resulting polariton modes are well described by a three-coupled-oscillator model. Even though only the cavity bonding mode intersects the CSVT of the polymer, coupling among all three composite modes must be explicitly treated. In particular, the character of the bonding mode for different aspect ratios of the cavity modifies the observed Rabi splitting occurring at 1732 cm^{-1}. The bonding mode carries the significant character of both composite modes while it intersects the CSVT for symmetric cavity geometries. The plasmon–plasmon interaction will dominate the plasmon–vibration interaction and reduce the L-M Rabi splitting. A two-oscillator model between the resulting bonding mode and CSVT was insufficient as it requires a different interaction potential, V_2, for each aspect ratio of the L-cavity. This is because such a model fails to account for the impact of both cavity arms on the plasmon–vibration interaction. When the bonding–antibonding avoided-crossing occurs for a similar L_x value as the intersection between the bonding mode and the CSVT, the L and M polariton branches have the significant character of all three composite modes: ω_x, ω_y, and ω_{vib}. These conditions correspond to symmetric cavity arm lengths. Under these conditions, since $V_1 > V_2$, the plasmon–plasmon interaction will dominate the plasmon–vibration interaction and reduce the L-M Rabi splitting. Only the multimode VSC model captures this behavior and can describe the system with fixed V_1 and V_2 for all aspect ratios.

The unique MIM L-cavity geometry employed here offers a number of advantages. The subwavelength confinement of the electromagnetic radiation and subsequent increase in the field intensity enable larger interaction potentials to the CSVT of the IP-Dip polymer with a reduced number of molecular vibrational oscillators as compared with an open cavity design [42]. Additionally, VSC is achieved with less than half the cavity volume of a typical square MIM cavity [42], indicating the large increase in field confinement compensates for the reduction in the number of vibrational oscillators. Unlike e-beam lithography, the 3D-printed nature of these cavities offers the ability to create complex cavity structures, such as creating nanoscopic channels in the insulator region to allow fluid to enter cavity region similar to the microfluidic Fabry–Perot cavity scheme discussed in Ref. [55]. So while the strong coupling to the CSVT of the IP-Dip polymer used during fabrication may not itself have technological relevance, it suggests the feasibility of schemes where VSC to other transitions is used for sensitive detection of analytes or to influence chemical reactions within solutions flowing through the 3D structure. The MIM L-cavities studied here have a volume of ~60 attoliters offering a platform for ultra-low-volume sensing of unique vibrational fingerprints.

Additionally, the VSC causes the polariton dominated by a vibrational character to borrow oscillator strength from the plasmon resonance, increasing its absorbance by five-fold, a fact that could be exploited for chemical or biological detection.

Strong coupling also enables the possibility to reversibly control the photochemical response and reaction rate of the material system inside the cavity [55], and unlike a reaction controlled by standard photochemistry, no photons are needed to modify a VSC-based chemical reaction as it occurs due to fluctuations in the vacuum field [37]. Moreover, as the MIM modes are angle independent and their dispersion is flat in momentum space, any chemical applications could occur at non-normal incidences, while other cavities with dispersion are limited to applications at normal incidences [55,56]. Nonlinear optical applications related to mid-infrared transitions, such as intersubband transitions of low-dimensional semiconductors, may also be possible if such materials could be introduced into the cavity [57].

The two plasmonic modes of interest in this study were the hybrid bonding and antibonding modes of this novel MIM L-cavity. We find that the polariton modes can be accurately modeled by the strongly coupled oscillator model in Eq. (B3) where the contributing resonances of each arm are given by the relation in Eq. (B1). While in this report, VSC required inclusion of a third oscillator associated with the CSVT, in the absence of such light–matter coupling, the L-cavity can be described using a two-coupled-oscillator model that considers only cavity modes of each arm. The L structure is one of the simplest in-plane anisotropic structures and has been used to manipulate the polarization of light and chiral responses to circularly polarized light [45–49]. Because the plasmonic modes of the L-cavity are composed of the coupled orthogonal modes of the two arms, it is expected that the L-cavity could exhibit circular dichroic behavior when the arms are anisotropic [58]. This cavity geometry could therefore offer the potential to couple to chiral vibrational modes in order to selectively detect or modify the behavior of one stereoisomer within a chiral enantiomer pair. Therefore, identifying and understanding any chiral response from these or similar laser-printed structures is a future direction for related work.

4. CONCLUSION

In summary, we demonstrated and characterized mid-IR multimode VSC in a nanoscale direct laser-printed MIM plasmonic nanogap cavity system. Such a fabrication scheme represents a cost-effective, highly accessible means of fabricating and rapidly evaluating mid-IR nanometer-sized plasmonic cavities that are capable of producing strong light–matter interactions in deep subwavelength volumes. The utilized 3D printing technique could allow for complex cavity designs, including those with voids for introducing solution samples for applications based on microfluidic platforms. Upon analysis of the L-shaped cavity electromagnetic response via analytical and EM simulations, we find that the fundamental dipole modes are a superposition of responses from each arm forming bonding and antibonding hybrid modes. Therefore, additional strong light–matter coupling to the CSVT of the polymer within the cavity requires a multimode coupled oscillator model for a more complete understanding of the system.

The three-coupled-oscillator system produces vibrational strong coupling between L and M polaritons and ultrastrong coupling between L/M and U polaritons with avoided-crossings that can only be fully understood by considering all three coupling potentials. These multifaceted optical cavities potentially provide a way to modify and control a material's chemical reactivity via VSC in novel ways due to its anisotropic multimodal optical response. For example, these structures could provide strong chiral fields to a particular chiral stereoisomer for the detection or selective chiral VSC-mediated chemistry. Additionally, the light–matter coupling strength is comparable to typical square-shaped MIM cavities but is achieved with half their volume. The vibrational mode absorption experiences a five-fold increase by borrowing oscillator strength from the plasmon modes. Therefore, this platform could be used for ultra-sensitive chemical detection across a wide bandwidth as the L-cavities support plasmon modes across the mid-IR into the near-IR while maintaining a low mode volume.

APPENDIX A: NUMERICAL MODELING

3D, full-wave, electromagnetic (EM) simulations were performed using the finite element method (COMSOL Multiphysics, wave optics module). The simulation domain was constructed using periodic Floquet boundary conditions in conjunction with a periodic port for injection of plane wave excitation and a perfectly matched layer region below the substrate to absorb any light transmitted through the Au film. The angle of incidence (AOI) was fixed at 22°—consistent with measurements. The domain cross section was set to

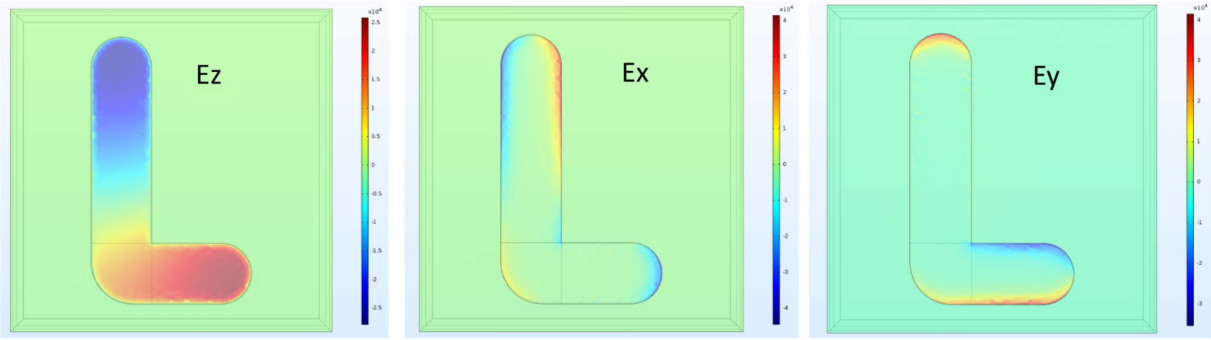

Fig. 5. E-field components of mode L in Fig. 2. Electric field mode (E_z, E_x, E_y) plots of mode L, E_z is also shown in Fig. 2(a).

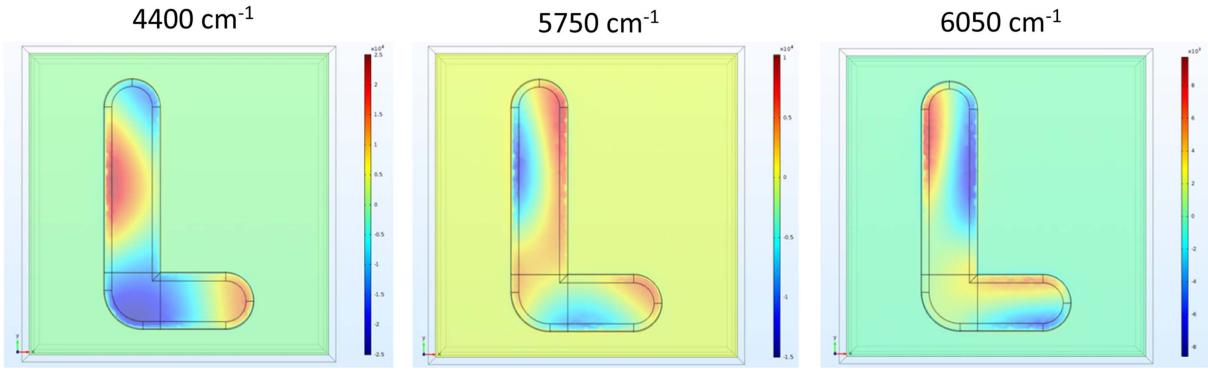

Fig. 6. Simulated reflectance spectra for L-antenna in Fig. 2. The field mode plots of higher-order modes are not characterized (5750 cm^{-1})/not seen (4400 and 6050 cm^{-1}) in the experimental data.

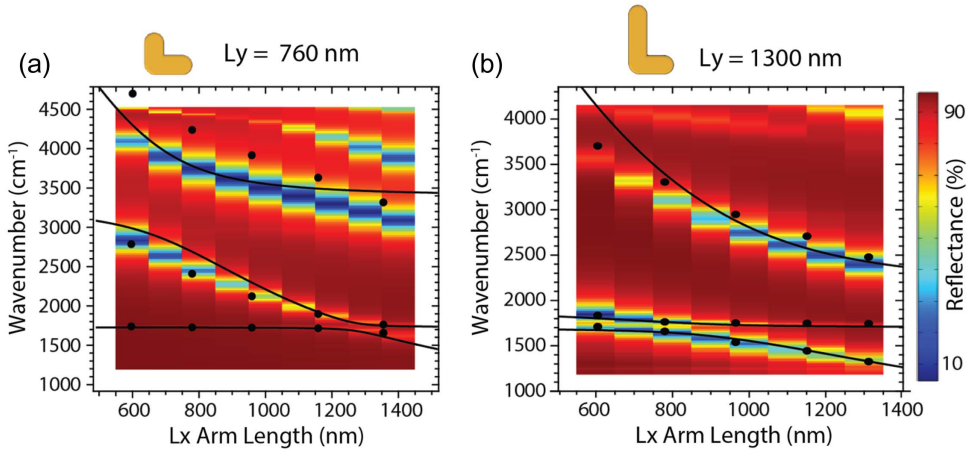

Fig. 7. Simulated reflectance as a function of L_x: (a) $L_y = 760$ nm and (b) $L_y = 1300$ cases overlaid on the experimental dip locations (black dots) and the polariton model (black lines) from Figs. 3(c) and 4(c).

1600 nm by 1600 nm corresponding to the nominal periodicity of the fabricated structures. The MIM L-cavities were approximated as rectangular planar films with the top corners of the evaporated Au and the IP-polymer layer rounded by an ROC of 50 nm. The tips of the arms were rounded by 150 nm, in accordance with the experimental SEM and AFM images as shown in Figs. 1(c) and 1(d). The IP-Dip polymer film thickness was set to 150 nm. An image of a simulated L-cavity is shown in Fig. 1(b). The dielectric constants for IP-Dip, silicon, and gold were taken from Refs. [59–61], respectively.

APPENDIX B: MODELING OF PLASMON RESPONSE AND VSC

In order to model the formation of the polariton modes (L, M, and U) of the system, we first need to model the L-cavity dipolar modes in the absence of VSC. As described above, the L-cavity can be thought of as two coupled cavities [49]. Each arm of the cavity can be treated as an independent oscillator, where a simple standing-wave condition can be used to analytically model the oscillator modes as a function of length. Thus, each MIM gap–plasmon arm has resonances given by

$$w\frac{2\pi}{\lambda}N_{\text{eff}} = m\pi + \phi, \tag{B1}$$

where w is the arm length of the cavity, λ is the free space wavelength of the excitation, m is the order of the mode, ϕ is the phase difference of the mode upon reflection at the termination boundaries, and N_{eff} is the effective mode index given by $N_{\text{eff}} = k_{\text{gap}}/k_o$. For small polymer thicknesses, t, one can use the approximation $\tanh(x) \cong x$, where $x = \sqrt{k_{\text{gap}}^2 - \varepsilon_d^2 k_o}\cdot\frac{t}{2}$. The wavenumber of the gap modes, k_{gap}, is then given by [11]

$$k_{\text{gap}} = k_0\sqrt{\varepsilon_d + \frac{1}{2}\left(\frac{k_{\text{gap}}^0}{k_o}\right)^2 + \sqrt{\left(\frac{k_{\text{gap}}^0}{k_o}\right)^2\left[\varepsilon_d - \varepsilon_m + \frac{1}{4}\left(\frac{k_{\text{gap}}^0}{k_o}\right)^2\right]}}, \tag{B2}$$

where k_o is the free-space wavenumber, ε_d and ε_m are the complex permittivity of the insulator and metal, respectively, and $k_{\text{gap}}^0 = -2\frac{\varepsilon_d}{t\varepsilon_m}$. Following the method described in Ref. [42] for modeling the uncoupled plasmonic modes, the IP-Dip Lorentzian and Gaussian transitions were removed from the ε_d obtained from Eq. (1) in Ref. [59]. The ε_m for Au was obtained from Ref. [61]. The phase difference ϕ is

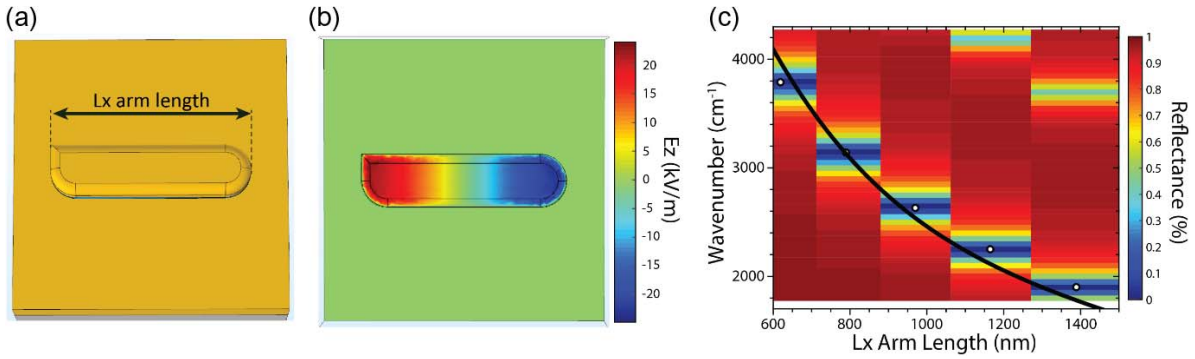

Fig. 8. Size-dependent modal dispersion of a single arm. (a) Geometry of a single arm ($L_x = 1165$ nm) used to simulate the dispersion in the contour plot of (b). (b) Field mode profile at 2250 cm^{-1} for $L_x = 1165$ nm. (c) Simulated reflectance spectra of the structures in (a) and (b) shown as a contour plot overlaid with the calculated dispersion of Eq. (B1).

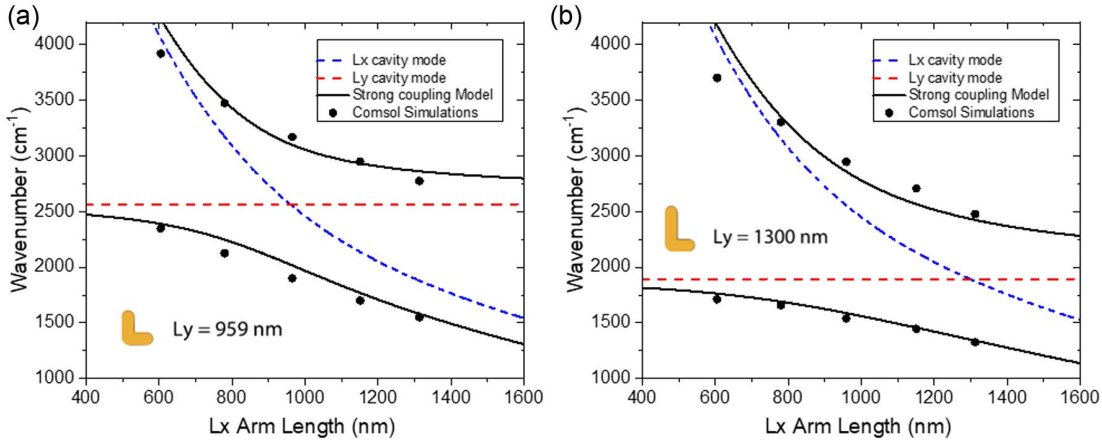

Fig. 9. Modeled L-cavity bonding and antibonding modes without the presence of the IP-Dip vibrational transitions. The L-cavity modes were simulated via COMSOL for various L_x while (a) $L_y = 956$ nm and (b) $L_y = 1300$ nm. The black solid lines are the bonding (lower) and antibonding (upper) modes modeled via a two-oscillator strong coupling model of the two uncoupled L_x and L_y cavity resonances associated with each arm (dashed lines). For this, Eq. (B3) is modified by setting plasmon–CSVT interaction potential to 0, $V_2 = 0$, and removing the CSVT, ω_{vib}. Thus, the eigenvalue problem is now given by the 2 × 2 matrix $\begin{bmatrix} \omega_x[x] & V_1 \\ V_1 & \omega_y \end{bmatrix}\begin{bmatrix} \alpha[x] \\ \beta[x] \end{bmatrix} = \lambda_{\pm}\begin{bmatrix} \alpha[x] \\ \beta[x] \end{bmatrix}$, where $\lambda_{\pm}$ are the eigenvalues of the system. The plasmon–plasmon interaction potential, V_1, was kept at 541 cm^{-1} as was found from Figs. 3 and 4.

dependent on the structural and material properties of the system and is related to the extent of the plasmon field that extends past the edges of the cavity [9]. To determine ϕ for this nonplanar system, Eq. (B1) is fitted to the EM simulated dispersion of a single arm resonance shown in Fig. 8. The best fit to Eq. (B1) is plotted in Fig. 8(c) and results in $\phi = -7.33°$. The resulting dispersion relation is then used to model the dipolar modes of the isolated arms L_y and L_x, indicated by the red and blue dashed curves in Fig. 3(b). Figure 9 shows the expected hybrid bonding and antibonding cavity modes of the two coupled arms without the presence of IP-Dip's CSVT. The hybrid modes were simulated via COMSOL and are in good agreement with the familiar coupled oscillator model applied to the two individual arm modes.

The VSC that gives rise to the polariton modes L, M, and U can be described by a set of linear coupled equations among three oscillators: the dipolar cavity mode of the L_x arm, ω_x, the dipolar cavity mode of the L_y arm, ω_y, and the CSVT of the IP-Dip polymer, ω_{vib}. The strongly coupled system is modeled in Figs. 3(b) and 4 with the multimode coupled oscillator model given by an eigenvalue equation with the 3 × 3 matrix $\boldsymbol{M}$ [35,62,63]:

$$\begin{bmatrix} \omega_x[x] & V_1 & V_2 \\ V_1 & \omega_y & V_2 \\ V_2 & V_2 & \omega_{\text{vib}} \end{bmatrix}\begin{bmatrix} \alpha[x] \\ \beta[x] \\ \gamma[x] \end{bmatrix} = \lambda_{\text{L,M,U}}\begin{bmatrix} \alpha[x] \\ \beta[x] \\ \gamma[x] \end{bmatrix}, \tag{B3}$$

with eigenvalues $\lambda_{\text{L,M,U}}$ given by $\det(\boldsymbol{M} - \lambda\boldsymbol{I}) = \boldsymbol{0}$:

$$\begin{aligned}&(\omega_x[x] - \lambda_{\text{L,M,U}})[(\omega_y - \lambda_{\text{L,M,U}})(\omega_{\text{vib}} - \lambda_{\text{L,M,U}}) - V_2^2] \\ &- V_1[V_1(\omega_{\text{vib}} - \lambda_{\text{L,M,U}}) - V_2^2] \\ &+ V_2[V_1V_2 - V_2(\omega_y - \lambda_{\text{L,M,U}})] \\ &= 0.\end{aligned} \tag{B4}$$

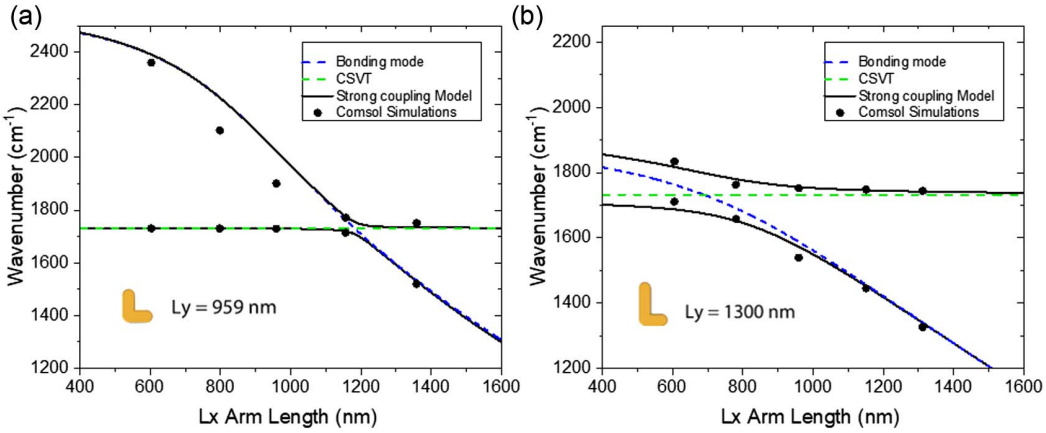

Fig. 10. Two-oscillator model prediction of the light–matter interaction. Predicted dispersion of two-oscillator model between the cavity bonding mode and the CSVT when (a) $L_y = 956$ nm and (b) $L_y = 1300$ nm. The dispersion of bonding mode is first modeled as described in Fig. 9. Then the coupling between CSVT and the bonding mode is fit to another two-coupled-oscillator model given by the 2×2 matrix $\begin{bmatrix} \omega_B[x] & V_2 \\ V_2 & \omega_{\text{vib}} \end{bmatrix} \begin{bmatrix} \alpha[x] \\ \beta[x] \end{bmatrix} = \lambda_{\pm} \begin{bmatrix} \alpha[x] \\ \beta[x] \end{bmatrix}$, where $\omega_B[x]$ is the bonding mode dispersion. The resulting interaction potentials are found to be $V_2 = 23$ cm^{-1} for (a) and $V_2 = 63$ cm^{-1} for (b).

Here, we explicitly consider three coupled oscillators: $\omega_x[x]$ is the dispersion of the plasmonic mode of the Lx arm as a function of length given by Eq. (B1); ω_y is the energy of the plasmonic mode for the Ly arm for a fixed average length; and ω_{vib} is the energy of the CSVT in wavenumbers (1732 cm^{-1}). The coupling strengths are determined by the interaction potentials $V_{1,2}$, where V_1 is the potential between the two cavity modes, $\omega_x[x]$ and ω_y, while coupling among the CSVT, ω_{vib}, and each of the cavity modes is given by V_2. Given the uniform thickness of the cavity, both cavity modes ω_x and ω_y are assumed to have equal interaction potentials with the CSVT ω_{vib}. The eigenvectors $\alpha[x], \beta[x], \gamma[x]$ are the Hopfield coefficients of the polariton system associated with $\omega_x[x], \omega_y, \omega_{\text{vib}}$, respectively, and describe how much vibrational or plasmonic character is present for each polariton mode.

APPENDIX C: OPTICAL CHARACTERIZATION

Polarized, mid-IR reflectance spectra were measured using an all-reflective, infrared microscope (Bruker Hyperion 1000)

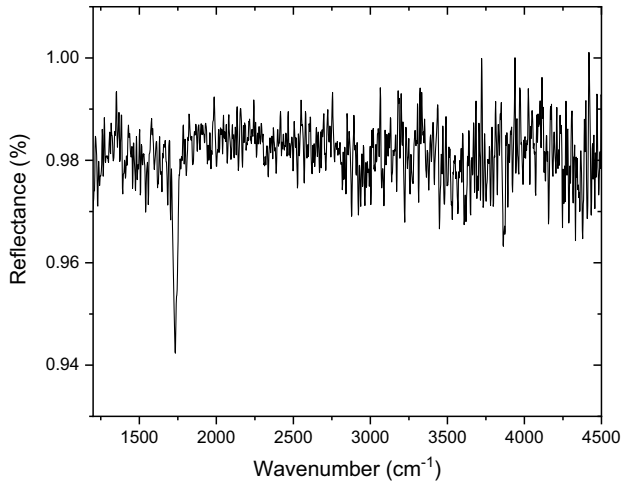

Fig. 12. FTIR reflectance spectra of bare IP-Dip on an Au subtrate. The absorbion of the IP-Dip CSVT can be seen at 1732 cm^{-1} with an FWHM of 32 cm^{-1}.

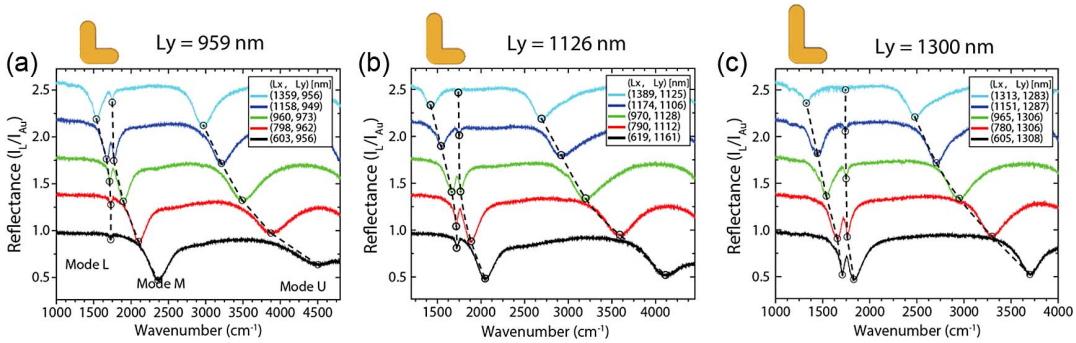

Fig. 11. Vibration-plasmon coupling for various L_y. (a)–(c) Waterfall plots of the experimental reflectance as L_x is varied for three different L_y: (a) 959 nm, (b) 1126 nm, and (c) 1300 nm. Modes L, M, and U are indicated in each plot by the dashed black lines.

coupled to an FTIR spectrometer (Bruker Vertex 80v). The microscope is outfitted with a wire-grid polarizer and 36× magnification reflective objective that illuminates the sample with polarized light having an average incident angle of 22°. The polarizer orientation is computer-controlled, and spectra were acquired with 5° increments of the polarization in order to obtain the polarization response of the measured samples.

Funding. Office of Naval Research (N0001421WX01075); U.S. Naval Research Laboratory Base Programs (1P76, 1P77).

Acknowledgment. The authors thank Dr. Igor Vurgaftman for helpful discussions concerning strong coupling. This work was supported by the Office of Naval Research through core programs at the U.S. Naval Research Laboratory (NRL) and the NRL Nanoscience Institute. This research was performed while N.V.P., M.A.M., and N.S. held NRC Research Associateship awards at the U.S. Naval Research Laboratory.

Disclosures. The authors declare no conflicts of interest.

Data Availability. Data underlying the results presented in this paper are not publicly available at this time but may be obtained from the authors upon reasonable request.

REFERENCES

1. M. Moskovits, "Surface-enhanced spectroscopy," Rev. Mod. Phys. **57**, 783–823 (1985).
2. M. Osawa, "Surface-enhanced infrared absorption," in *Near-Field Optics and Surface Plasmon Polaritons* (Springer, 2001), pp. 163–187.
3. C. K. Chen, A. R. B. De Castro, and Y. R. Shen, "Surface-enhanced second-harmonic generation," Phys. Rev. Lett. **46**, 145–148 (1981).
4. I. Gontijo, M. Boroditsky, E. Yablonovitch, S. Keller, U. K. Mishra, S. P. DenBaars, and M. Krames, "Coupling of InGaN quantum well photoluminescence to silver surface plasmons," Phys. Rev. B **60**, 11564–11567 (1999).
5. N. Kinsey, M. Ferrera, V. M. Shalaev, and A. Boltasseva, "Examining nanophotonics for integrated hybrid systems: a review of plasmonic interconnects and modulators using traditional and alternative materials [Invited]," J. Opt. Soc. Am. B **32**, 121–142 (2015).
6. C. Tserkezis, R. Esteban, D. O. Sigle, J. Mertens, L. O. Herrmann, J. J. Baumberg, and J. Aizpurua, "Hybridization of plasmonic antenna and cavity modes: extreme optics of nanoparticle-on-mirror nanogaps," Phys. Rev. A **92**, 053811 (2015).
7. J. J. Baumberg, J. Aizpurua, M. H. Mikkelsen, and D. R. Smith, "Extreme nanophotonics from ultrathin metallic gaps," Nat. Mater. **18**, 668–678 (2019).
8. Y. Fang and M. Sun, "Nanoplasmonic waveguides: towards applications in integrated nanophotonic circuits," Light Sci. Appl. **4**, e294 (2015).
9. M. G. Nielsen, D. K. Gramotnev, A. Pors, O. Albrektsen, and S. I. Bozhevolnyi, "Continuous layer gap plasmon resonators," Opt. Express **19**, 19310–19322 (2011).
10. E. N. Economou, "Surface plasmons in thin films," Phys. Rev. **182**, 539–554 (1969).
11. S. I. Bozhevolnyi and T. Søndergaard, "General properties of slow-plasmon resonant nanostructures: nano-antennas and resonators," Opt. Express **15**, 10869–10877 (2007).
12. G. Duffett, R. Wirth, M. Rayer, E. R. Martins, and T. F. Krauss, "Metal-insulator-metal nanoresonators-strongly confined modes for high surface sensitivity," Nanophotonics **9**, 1547–1552 (2020).
13. N. Liu, M. Mesch, T. Weiss, M. Hentschel, and H. Giessen, "Infrared perfect absorber and its application as plasmonic sensor," Nano Lett. **10**, 2342–2348 (2010).
14. A. Cattoni, P. Ghenuche, A. M. Haghiri-Gosnet, D. Decanini, J. Chen, J. L. Pelouard, and S. Collin, "λ^3/1000 plasmonic nanocavities for biosensing fabricated by soft UV nanoimprint lithography," Nano Lett. **11**, 3557–3563 (2011).
15. Y. Luo, G. D. Shepard, J. V. Ardelean, D. A. Rhodes, B. Kim, K. Barmak, J. C. Hone, and S. Strauf, "Deterministic coupling of site-controlled quantum emitters in monolayer WSe_2 to plasmonic nanocavities," Nat. Nanotechnol. **13**, 1137–1142 (2018).
16. J. J. Greffet, M. Laroche, and F. Marquier, "Impedance of a nanoantenna and a single quantum emitter," Phys. Rev. Lett. **105**, 117701 (2010).
17. M. T. Hill, M. Marell, E. S. P. Leong, B. Smalbrugge, Y. Zhu, M. Sun, P. J. van Veldhoven, E. J. Geluk, F. Karouta, Y.-S. Oei, R. Nötzel, C.-Z. Ning, M. K. Smit, R. Zia, M. D. Selker, P. B. Catrysse, and M. L. Brongersma, "Lasing in metal-insulator-metal sub-wavelength plasmonic waveguides," Opt. Express **17**, 11107–11112 (2009).
18. A. Rose, T. B. Hoang, F. McGuire, J. J. Mock, C. Ciracì, D. R. Smith, and M. H. Mikkelsen, "Control of radiative processes using tunable plasmonic nanopatch antennas," Nano Lett. **14**, 4797–4802 (2014).
19. J. Huang, G. M. Akselrod, T. Ming, J. Kong, and M. H. Mikkelsen, "Tailored emission spectrum of 2D semiconductors using plasmonic nanocavities," ACS Photon. **5**, 552–558 (2018).
20. J. Sun, H. Hu, D. Pan, S. Zhang, and H. Xu, "Selectively depopulating valley-polarized excitons in monolayer MoS_2 by local chirality in single plasmonic nanocavity," Nano Lett. **20**, 4953–4959 (2020).
21. C. Weisbuch, M. Nishioka, A. Ishikawa, and Y. Arakawa, "Observation of the coupled exciton-photon mode splitting in a semiconductor quantum microcavity," Phys. Rev. Lett. **69**, 3314–3317 (1992).
22. V. M. Agranovich, M. Litinskaia, and D. G. Lidzey, "Cavity polaritons in microcavities containing disordered organic semiconductors," Phys. Rev. B **67**, 085311 (2003).
23. X. Liu, T. Galfsky, Z. Sun, F. Xia, E. C. Lin, Y. H. Lee, S. Kéna-Cohen, and V. M. Menon, "Strong light-matter coupling in two-dimensional atomic crystals," Nat. Photonics **9**, 30–34 (2015).
24. X. Yu, Y. Yuan, J. Xu, K. T. Yong, J. Qu, and J. Song, "Strong coupling in microcavity structures: principle, design, and practical application," Laser Photon. Rev. **13**, 1800219 (2018).
25. L.-C. Kwek, A. Auffeves, D. Gerace, M. Richard, S. Portolan, M. F. Santos, and C. Miniature, *STRONG LIGHT- From Atoms to Solid-State Systems* (World Scientific, 2013).
26. G. Khitrova, H. M. Gibbs, M. Kira, S. W. Koch, and A. Scherer, "Vacuum Rabi splitting in semiconductors," Nat. Phys. **2**, 81–90 (2006).
27. P. Törmö and W. L. Barnes, "Strong coupling between surface plasmon polaritons and emitters: a review," Rep. Prog. Phys. **78**, 013901 (2015).
28. D. G. Baranov, M. Wersäll, J. Cuadra, T. J. Antosiewicz, and T. Shegai, "Novel nanostructures and materials for strong light-matter interactions," ACS Photon. **5**, 24–42 (2018).
29. D. E. Gómez, K. C. Vernon, P. Mulvaney, and T. J. Davis, "Surface plasmon mediated strong exciton-photon coupling in semiconductor nanocrystals," Nano Lett. **10**, 274–278 (2010).
30. J. P. Long and B. S. Simpkins, "Coherent coupling between a molecular vibration and Fabry-Perot optical cavity to give hybridized states in the strong coupling limit," ACS Photon. **2**, 130–136 (2015).
31. H. Memmi, O. Benson, S. Sadofev, and S. Kalusniak, "strong coupling between surface plasmon polaritons and molecular vibrations," Phys. Rev. Lett. **118**, 126802 (2017).
32. J. Wang, K. Yu, Y. Yang, G. V. Hartland, J. E. Sader, and G. P. Wang, "Strong vibrational coupling in room temperature plasmonic resonators," Nat. Commun. **10**, 1527 (2019).
33. T. Chervy, A. Thomas, E. Akiki, R. M. A. Vergauwe, A. Shalabney, J. George, E. Devaux, J. A. Hutchison, C. Genet, and T. W. Ebbesen, "Vibro-polaritonic IR emission in the strong coupling regime," ACS Photon. **5**, 217–224 (2018).
34. A. D. Dunkelberger, B. T. Spann, K. P. Fears, B. S. Simpkins, and J. C. Owrutsky, "Modified relaxation dynamics and coherent energy

exchange in coupled vibration-cavity polaritons," Nat. Commun. **7**, 13504 (2016).
35. W. Ahn, I. Vurgaftman, A. D. Dunkelberger, J. C. Owrutsky, and B. S. Simpkins, "Vibrational strong coupling controlled by spatial distribution of molecules within the optical cavity," ACS Photon. **5**, 158–166 (2018).
36. K. Joseph, S. Kushida, E. Smarsly, D. Ihiawakrim, A. Thomas, G. L. Paravicini-Bagliani, K. Nagarajan, R. Vergauwe, E. Devaux, O. Ersen, U. H. F. Bunz, and T. W. Ebbesen, "Supramolecular assembly of conjugated polymers under vibrational strong coupling," Angew. Chem. Int. Ed. **60**, 19665–19670 (2021).
37. J. A. Hutchison, T. Schwartz, C. Genet, E. Devaux, and T. W. Ebbesen, "Modifying chemical landscapes by coupling to vacuum fields," Angew. Chem. Int. Ed. **51**, 1592–1596 (2012).
38. A. Thomas, J. George, A. Shalabney, M. Dryzhakov, S. J. Varma, J. Moran, T. Chervy, X. Zhong, E. Devaux, C. Genet, J. A. Hutchison, and T. W. Ebbesen, "Ground-state chemical reactivity under vibrational coupling to the vacuum electromagnetic field," Angew. Chem. Int. Ed. **55**, 11462–11466 (2016).
39. A. Braun and S. A. Maier, "Versatile direct laser writing lithography technique for surface enhanced infrared spectroscopy sensors," ACS Sens. **1**, 1155–1162 (2016).
40. F. Verdelli, J. J. P. M. Schulpen, A. Baldi, and J. G. Rivas, "Chasing vibro-polariton fingerprints in infrared and raman spectra using surface lattice resonances on extended metasurfaces," J. Phys. Chem. C **126**, 7143–7151 (2022).
41. K. S. Menghrajani, G. R. Nash, and W. L. Barnes, "Vibrational strong coupling with surface plasmons and the presence of surface plasmon stop bands," ACS Photon. **6**, 2110–2116 (2019).
42. G. Dayal, I. Morichika, and S. Ashihara, "Vibrational strong coupling in subwavelength nanogap patch antenna at the single resonator level," J. Phys. Chem. Lett. **12**, 3171–3175 (2021).
43. M. Deubel, G. Von Freymann, M. Wegener, S. Pereira, K. Busch, and C. M. Soukoulis, "Direct laser writing of three-dimensional photonic-crystal templates for telecommunications," Nat. Mater. **3**, 444–447 (2004).
44. P. I. Dietrich, M. Blaicher, I. Reuter, M. Billah, T. Hoose, A. Hofmann, C. Caer, R. Dangel, B. Offrein, U. Troppenz, M. Moehrle, W. Freude, and C. Koos, "*In situ* 3D nanoprinting of free-form coupling elements for hybrid photonic integration," Nat. Photonics **12**, 241–247 (2018).
45. J. Sung, E. M. Hicks, R. P. Van Duyne, and K. Spears, "Nanoparticle spectroscopy: plasmon coupling in finite-sized two-dimensional arrays of cylindrical silver nanoparticles," J. Phys. Chem. C **112**, 4091–4096 (2008).
46. Q. Lévesque, M. Makhsiyan, P. Bouchon, F. Pardo, J. Jaeck, N. Bardou, C. Dupuis, R. Haïdar, and J. L. Pelouard, "Plasmonic planar antenna for wideband and efficient linear polarization conversion," Appl. Phys. Lett. **104**, 111105 (2014).
47. J. Yang and J. Zhang, "Nano-polarization-converter based on magnetic plasmon resonance excitation in an L-shaped slot antenna," Opt. Express **21**, 7934–7942 (2013).
48. R. Blanchard, G. Aoust, P. Genevet, N. Yu, M. A. Kats, Z. Gaburro, and F. Capasso, "Modeling nanoscale V-shaped antennas for the design of optical phased arrays," Phys. Rev. B **85**, 155457 (2012).
49. L. J. Black, Y. Wang, C. H. De Groot, A. Arbouet, and O. L. Muskens, "Optimal polarization conversion in coupled dimer plasmonic nanoantennas for metasurfaces," ACS Nano **8**, 6390–6399 (2014).
50. K. S. Menghrajani, H. A. Fernandez, G. R. Nash, and W. L. Barnes, "Hybridization of multiple vibrational modes via strong coupling using confined light fields," Adv. Opt. Mater. **7**, 1900403 (2019).
51. I. Imran, G. E. Nicolai, N. D. Stavinski, and J. R. Sparks, "Tuning vibrational strong coupling with co-resonators," ACS Photon. **6**, 2405–2412 (2019).
52. Z. T. Brawley, S. D. Storm, D. A. C. Mora, M. Pelton, and M. Sheldon, "Angle-independent plasmonic substrates for multi-mode vibrational strong coupling with molecular thin films," J. Chem. Phys. **154**, 104305 (2021).
53. K. Chen, R. Adato, and H. Altug, "Dual-band perfect absorber for multispectral plasmon-enhanced infrared spectroscopy," ACS Nano **6**, 7998–8006 (2012).
54. Y. Liu, Z. Zhu, J. Qian, J. Yuan, J. Yan, Z. X. Shen, and L. Jiang, "Strong coupling between two-dimensional transition metal dichalcogenides and plasmonic-optical hybrid resonators," Phys. Rev. B **104**, 205118 (2021).
55. K. Nagarajan, A. Thomas, and T. W. Ebbesen, "Chemistry under vibrational strong coupling," J. Am. Chem. Soc. **143**, 16877–16889 (2021).
56. T. E. Li, A. Nitzan, and J. E. Subotnik, "Collective vibrational strong coupling effects on molecular vibrational relaxation and energy transfer: numerical insights via cavity molecular dynamics simulations," Angew. Chem. Int. Ed. **60**, 15533–15540 (2021).
57. J. Lee, M. Tymchenko, C. Argyropoulos, P. Y. Chen, F. Lu, F. Demmerle, G. Boehm, M. C. Amann, A. Alù, and M. A. Belkin, "Giant nonlinear response from plasmonic metasurfaces coupled to intersubband transitions," Nature **511**, 65–69 (2014).
58. X. T. Kong, L. K. Khorashad, Z. Wang, and A. O. Govorov, "Photothermal circular dichroism induced by plasmon resonances in chiral metamaterial absorbers and bolometers," Nano Lett. **18**, 2001–2008 (2018).
59. D. B. Fullager, G. D. Boreman, and T. Hofmann, "Infrared dielectric response of nanoscribe IP-dip and IP-L monomers after polymerization from 250 cm^{-1} to 6000 cm^{-1}," Opt. Mater. Express **7**, 888–894 (2017).
60. H. H. Li, "Refractive index of silicon and germanium and its wavelength and temperature derivatives," J. Phys. Chem. Ref. Data **9**, 561–658 (1980).
61. E. D. Palik, *Handbook of Optical Constants of Solids* (Academic Press, 1997).
62. V. Savona, L. C. Andreani, P. Schwendimann, and A. Quattropani, "Quantum well excitons in semiconductor microcavities: unified treatment of weak and strong coupling regimes," Solid State Commun. **93**, 733–739 (1995).
63. R. Deshmukh, P. Marques, A. Panda, M. Y. Sfeir, S. R. Forrest, and V. M. Menon, "Modifying the spectral weights of vibronic transitions via strong coupling to surface plasmons," ACS Photon. **7**, 43–48 (2020).